A study on the buckling behaviour of aluminium alloy sheet in deep drawing with macro-textured blankholder

Zheng, Kailun; Politis, Denis J.; Lin, Jianguo; Dean, Trevor A.

DOI:
10.1016/j.ijmecsci.2016.03.011

Document Version
Peer reviewed version

Citation for published version (Harvard):
Zheng, K, Politis, DJ, Lin, J & Dean, TA 2016, 'A study on the buckling behaviour of aluminium alloy sheet in deep drawing with macro-textured blankholder', *International Journal of Mechanical Sciences*, vol. 110, pp. 138-150. https://doi.org/10.1016/j.ijmecsci.2016.03.011

A study on the buckling behaviour of aluminium alloy sheet in deep drawing with macro-textured blankholder

Kailun Zheng, Denis J. Politis, Jianguo Lin, Trevor A. Dean

www.elsevier.com/locate/ijmecsci

PII: S0020-7403(16)00091-6
DOI: http://dx.doi.org/10.1016/j.ijmecsci.2016.03.011
Reference: MS3251

To appear in: *International Journal of Mechanical Sciences*

Received date: 1 February 2016
Accepted date: 9 March 2016

Cite this article as: Kailun Zheng, Denis J. Politis, Jianguo Lin and Trevor A Dean, A study on the buckling behaviour of aluminium alloy sheet in deep drawing with macro-textured blankholder, *International Journal of Mechanical Sciences,* http://dx.doi.org/10.1016/j.ijmecsci.2016.03.011

A study on the buckling behaviour of aluminium alloy sheet in deep drawing with macro-textured blankholder

Kailun Zheng [a)], Denis J. Politis [a)], Jianguo Lin [a)], Trevor A. Dean [b)]

[a] Department of Mechanical Engineering, Imperial College London, Exhibition Road, London SW7 2AZ, UK

[b] School of Mechanical Engineering, University of Birmingham, Edgbaston, Birmingham B15 2TT, UK

Abstract

In this paper an experimental, numerical and analytical investigation is presented of the wrinkling behaviour that occurs in the flange of deep drawn cylindrical cups of aluminium alloy sheet using macro-textured blankholder surfaces. A series of deep drawing experiments were performed using a range of tool textures, draw ratios and blank-holding forces. A numerical material and process model was formulated to enable the occurrence of wrinkling to be simulated. In addition, two analytical buckling models of aluminium alloy sheet in deep drawing with macro-textured blankholder based on the energy method, (namely a one-dimensional and two-dimensional model) were developed for the first-time and utilised to predict the effect of process parameters on wrinkling. The analytical buckling models investigated two boundary conditions, hinged and built-in boundary condition. It was found that texture geometry and draw ratio had a significant effect on wrinkling but the blank-holding force did not. The analytical models developed in this paper to represent sheet metal wrinkling behaviour for the macro-textured tools can be used as a design guide to determine the geometry of tool textures necessary to avoid wrinkling defects in aluminium alloy stamping processes.

Keywords: Aluminium stamping, macro-textured tool, FE model, flange wrinkling, buckling model

Corresponding Author: D. J. Politis: denis.politis06@imperial.ac.uk

1. Introduction

With the increasing demand for fuel economy and emissions reduction in the automotive and aircraft industries, light-weight alloys such as aluminium alloy and magnesium alloy, have become popular candidates in recent years to replace traditional steel alloy [1-3]. To overcome the poor ductility when forming aluminium alloy at room temperature, Lin et al. proposed a hot stamping process, known as "solution Heat treatment, cold die Forming and Quenching" (HFQ^{TM}) [4]. In this process, heat treatable aluminium alloy work-pieces are heated to and then hot stamped at solution heat treatment temperature and simultaneously quenched within cold dies [5]. Subsequently, the formed components can be artificially aged to obtain maximum strength [6]. As the HFQ process is a non-isothermal process, and a high friction coefficient is typically observed at elevated temperatures [7], the thermal and tribological properties at the tool/work-piece interface significantly affect formability in the forming process [8-9].

Tribology in hot stamping of aluminium alloys can be improved through surface treatments, such as the application of coatings and textures, which can reduce friction coefficient directly and indirectly [10-11]. Costa and Hutchings [12-13] found that friction was significantly reduced through the use of patterned tool surfaces in strip drawing processes, where these grooves were believed to act as lubricant reservoirs to enhance the lubrication effect. Zheng et al. [14] investigated hot stamping processes of aluminium alloys using macro-textured tools, which enabled the blank temperature at the flange area to be relatively preserved, with a significant increase in draw-ability being observed due to a more uniform temperature distribution throughout the blank. However, for components with complex geometry, macro-textures may cause wrinkling in the flange area due to the absence of blank-holding contact in the region of a texture hollow. In order to take advantage of the benefits of tool textures whilst avoiding wrinkling, an understanding of the parameters involved in the onset of wrinkling must be studied.

To this end, extensive research has been conducted to enable prediction of the onset of wrinkling. Geckeler [15] proposed a mathematical analysis for wrinkling behaviour in the deep drawing process without blankholder, using which, the critical stress and wrinkling wave number can be determined. Senior [16] extended Geckeler's results using an energy method, in his research, the circular flange was assumed as a one-dimensional beam, buckling occurred when the compressive stress in the circumferential direction reached a critical value. The above research was based on the assumption of one-dimensional beam theory, which although simple to calculate, would not accurately reflect a flange of large flange, and hence is useful only when the width of the flange is small compared to the radius of blank [17]. Yu and Johnson [18] applied the energy method based on an assumption of two-dimensional elastic-based rigid-plastic stability theory to analyse wrinkling behaviour in the deep drawing process. An analytical buckling model was established and the onset of wrinkling and wave number were predicted. In recent years, Hutchinson [19-20] proposed a bifurcation function based on Hill's general theory of uniqueness and bifurcation in elastic-plastic solids [21]. This function can be given as in Eq. (1):

$$F = \int_s \left\{ \dot{M}_{ij}\dot{\kappa}_{ij} + \dot{N}_{ij}\dot{\varepsilon}^s_{ij} + N_{ij}\dot{\omega}_{,i}\dot{\omega}_{,j} \right\} ds \tag{1}$$

In this equation, s represents the middle surface region where wrinkling appears, $\dot{N}_{ij}$ and $\dot{M}_{ij}$ represent the stress resultants and stress couples (per unit width), $\dot{\kappa}_{ij}$ the bending strain

tensor, $\dot{\varepsilon}_{ij}^{s}$ the stretch strain tensor, and $\dot{\omega}$ represents the buckling displacement normal to the middle surface. On the right hand side of Eq. (1), the first item represents the bending energy $(i = j)$ and twisting energy $(i \neq j)$, the second term is the strain energy due to membrane stresses, and the third term may be interpreted as the potential energy of the edge stress or the work done by the applied in-plane stresses in the middle surface. For this equation, the value of $F = 0$ corresponds to the critical condition for wrinkles to occur. Wang et al. [22] further extended this buckling model by considering the anisotropic property of test-piece material in sheet metal forming processes, and Hill's non-quadratic yielding criterion was introduced to replace the Mises yielding criterion. Correia et al. [23] also investigated wrinkling of anisotropic metal sheets and established a model based on bifurcation theory to predict the initiation of wrinkling in the wall zone of conical cup tests, and corresponding FE simulations were compared with the predictions of the bifurcation model. Cao et al. [24-25] proposed a C-B wrinkling criterion based on energy conservation principals which considered the blank-holder effect, and experimental validations on this model were performed using a rectangular shaped component. Wang et al. [26] applied a differential quadrature method to investigate the buckling of rectangular plates under either uniaxial or biaxial compressive point loads with the consideration of different boundary conditions. Most of the above buckling model analyses and assumptions were based on whole flange areas with or without blank-holding force constraint. For the use of macro-textured tool surfaces with varying texture dimensions, alternative assumptions may be required, which the work described in this paper is designed to determine.

Wrinkling behaviour that occurs during a stamping process when using macro-textured tooling is investigated experimentally, numerically and analytically. A deep drawing experiment with macro-textured tooling and corresponding FE simulation were performed. Two analytical buckling models using the energy method specifically for macro-textured tools are established and validated by experimental results. The one-dimensional beam and two-dimensional plate elastic-plastic assumption were reviewed and applied to different texture tool dimensions. The effects of blank-holding force, boundary conditions, texture ratio and draw ratio on the occurrence of flange wrinkling were investigated.

2. Experimental set-up

2.1 Material and test-piece

Commercial AA6082-T6 aluminium alloy sheet with a thickness of 1.5 mm was used as the test-piece material. The chemical composition of the alloy is shown in Tab. 1 [27]. A standard annealing heat treatment as described in Section 2.3 was performed for the test-pieces in order to improve ductility and reduce anisotropic character of the as-rolled T6 raw material [28].

Tab. 1. Chemical composition of AA6082 [27]

Element	Mn	Fe	Mg	Si	Cu	Zn	Ti	Cr	Al
%	0.4-1.0	0-0.5	0.6-1.2	0.7-1.3	0-0.1	0-0.2	0-0.1	0-0.25	Balance

Circular test-pieces with diameters: 170, 180 and 190 mm were produced by laser cutting. A punch diameter of 100 mm was used for the deep drawing experiments thus providing draw ratios ($DR = D_{blank} / D_{punch}$) of 1.7, 1.8 and 1.9 respectively.

2.2 Experimental set-up and tool preparation

To investigate wrinkling behaviour during stamping processes using macro-textured tool surfaces, a classical deep drawing process was used and Fig.1 (a) shows the set-up of the test rig made of G3500 cast iron. The tool set was mounted on a 250 kN ESH hydraulic press with a maximum forming speed of 500 mm/s and a total stroke of 200 mm. The flat nosed 100 mm cylindrical punch, with a 10mm corner radius, was attached to the machine bed through a support column and load cell and the die, with a 10 mm entrance radius, was attached to the press slide. The blankholder was supported on gas springs which could exert a maximum force of 300 kN. Four different blankholder surfaces were used, a plane surface and three macro-textured surfaces comprising radial grooves of rectangular cross-section of different dimensions as shown in Fig.1 (b). The variable forming speed was recorded on an oscilloscope. The formed part was removed from the punch using an ejector in the punch nose. In order to remove the formed part post-forming, an ejector was designed, enabling the part to be separated from the punch via the application of a force (***F***) through the channels within this punch. The horizontal die surface was flat without a machined macro-texture. The clearance between the die and punch was 0.1 times of test-piece thickness.

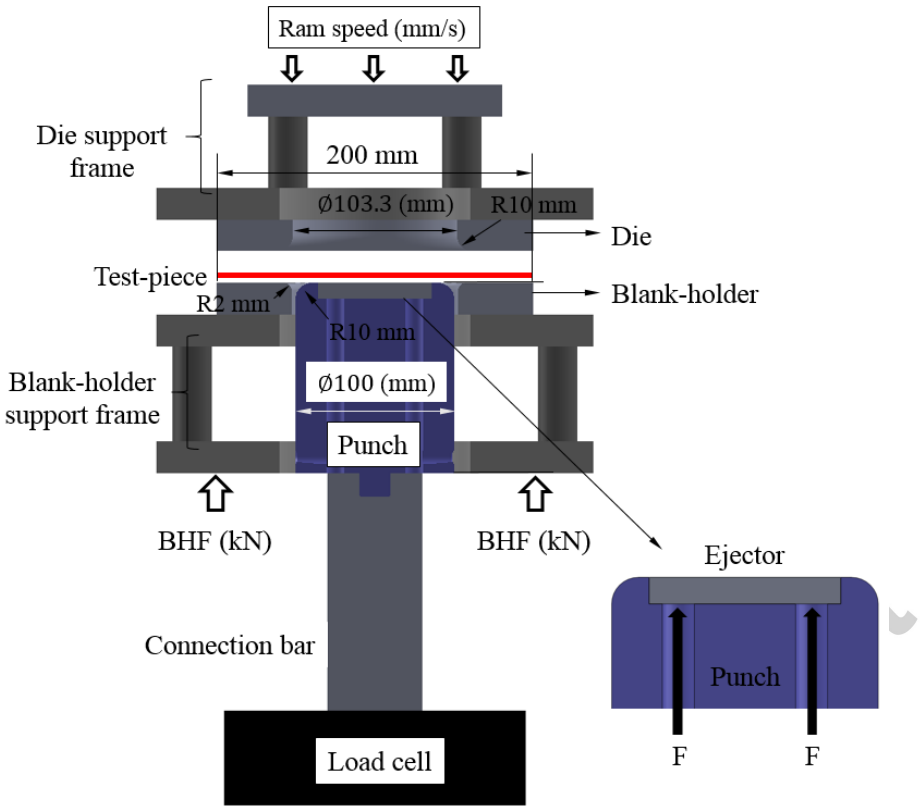

(a) Schematic design of the tool set

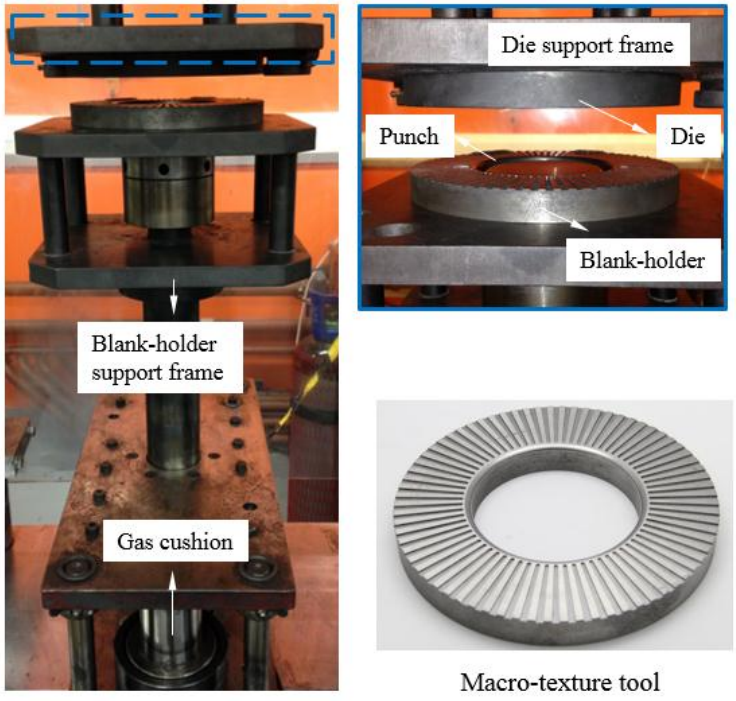

(b) Tool set and macro-textured blankholder

Fig.1. The deep drawing tool set

Fig.2 shows the design of the macro-textured blankholder tool surfaces presented in Fig.1 (b). Macro-textures were machined on blankholder surfaces in the radial direction to avoid the constraint effect if the macro-textures are not parallel with material flow direction [14], using CNC milling and related to function, and can be divided into two features: groove and surface. The depth of each groove, which did not contact the test-piece, was 1 mm. The size of each feature was defined by the radial angle each subtended. Arc angles of surface and groove are defined as θ_S and θ_G respectively and the texture ratio was defined as in Eq. (2) which is equal to the ratio between the groove and surface arc angles. The texture ratio $\alpha = 0$ represented the full contact between tool and test-piece (flat blankholder surface). In this paper, texture ratios of α = 0, 1, 3 and 5 were used.

$$\alpha = \theta_G / \theta_S \tag{2}$$

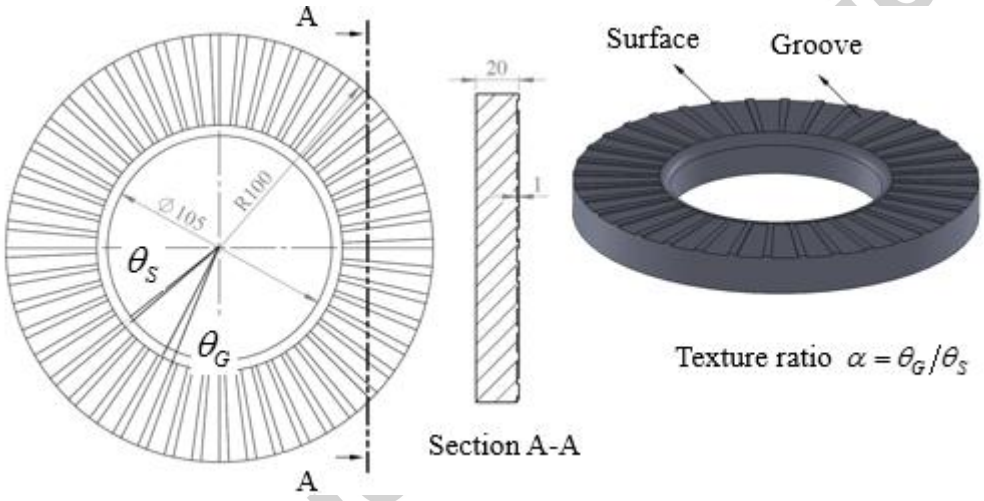

Fig.2. Macro-texture tool surfaces and texture definition

2.3 Test procedure

The test-piece material was first annealed by heating to 415 °C for one hour and subsequently furnace cooling to room temperature. These annealed test-pieces were cold stamped using macro-textured blankholders of texture ratios 0, 1, 3 and 5. Blank-holding force was adjusted through the gas springs then the annealed test-pieces with different draw ratios (1.7, 1.8 and 1.9) were positioned concentrically on blankholders lubricated with Omega-35 lubricant. Punch and die surfaces were also lubricated before each test. After test-piece positioning, the press was activated and the ram moved downwards at a ram speed of 75 mm/s to draw the test-piece into the die for chosen depths. Formed cups were ejected from the punch and characteristics of the flanges were then measured.

3. Numerical modelling

3.1 FE model and simulation set-up

FE simulations were performed for a range of macro-textured blankholders to investigate the occurrence of wrinkling behaviour and material deformation during the deep drawing process. The simulations were performed using a commercial finite element software Pamstamp 2G 2015.0. The FE model of the deep drawing process, including the test-piece, blankholder texture, circular flat punch and die profile as well as the dimensions, loading and boundary conditions are shown in Fig. 3.

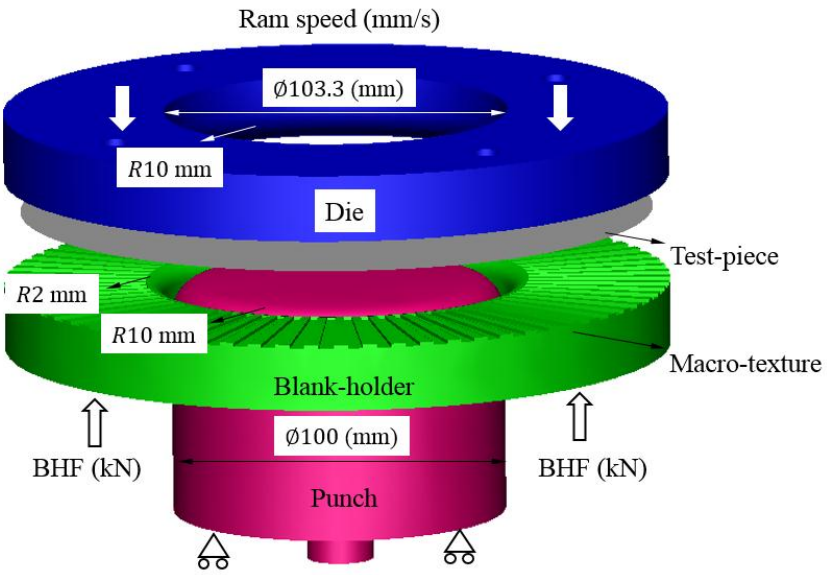

Fig.3. FE model and simulation set up

For the test-piece material, shell elements (Belytschoko-Tsay) were used. The mesh size is fixed as 2 mm, and the number of test-piece elements used was 16640, 18496 and 20448 for draw ratio 1.7, 1.8 and 1.9 respectively. Tool mesh selected was default solid elements in Pamstamp. The number of tool elements used were 3348, 5443 and 5431 for the punch, die and blankholder (full contact case) respectively. To improve the simulation efficiency, tools were treated as rigid bodies and no mass scaling was used in the simulations. The process parameters used for the simulations are given in Tab.2.

Tab. 2. Process parameters in FE simulation

Process parameters	Values
Blankholder texture ratio	0, 1, 3 and 5
Draw ratio	1.7, 1.8 and 1.9
Blank-holding force (kN)	10, 40
Forming speed (mm/s)	75

To model the constitutive relationship of AA6082-O condition, the stress-strain data of this material was obtained from uniaxial tensile tests performed using the Instron testing system. The obtained experimental data were input into Pamstamp via look up table. The whole stamping process was performed at room temperature, thus no heat transfer effect was considered. The element type selected for the blank was Belytschoko-Tsay with one integration point at the mid-plane in order to improve simulation efficiency without significant loss to numerical accuracy. Other material properties such as density, Young's modulus and Poisson ratio were applied as: 2.7 E-9 tonne/mm^3, 70GPa, 0.33 for aluminium alloy and 7.5 E-9 tonne/mm^3, 130GPa, 0.3 for tool material (cast iron). The friction coefficient in the simulation were selected as $\mu = 0.09$ between aluminium alloy and cast iron at room temperature which is obtained from pin on disk friction coefficient tests using Omega-35 lubricant.

The FE simulation follows the experimental procedure and is divided into two stages; blank positioning and blank stamping. In the blank positioning stage, the encastre boundary condition was applied on the punch to restrict all degrees of freedom. The test-piece was positioned on the blankholder, using an implicit convergence test to determine the end of blank positioning stage. When the blank is positioned, the die moves downwards vertically in the z direction to deform the test-piece, an explicit calculation method was applied for this stage. During this stage, the encastre boundary was still used for the punch, while the die and blankholder were free in the vertical direction (z direction). The end of the stamping stage was controlled by the stroke of die. In the simulations, the maximum die stroke can satisfy the fully drawn in test-piece.

3.2 FE model verification

The validations of the FE model were performed from two aspects, one was the occurrence of wrinkling using different macro-textured blankholders and the other by comparing the normalized thickness variations in Eq. (3) between experimental and computed parts with different draw ratios and blankholders. Fig.4 shows typical formed parts using different tool texture ratios: (a) $\alpha = 1$ and (b) $\alpha = 3$. With regard to the wrinkling occurrence, using a relevant smaller texture ratio blankholder (a), the test-piece could be fully drawn in, the character of wave edges could be seen both from the experimental and computational results. When using a larger texture ratio blankholder (b), the test-piece is drawn to a certain depth and wrinkling occurs in the flange. Hence it is seen that the wrinkling occurrence using blankholders with different texture-ratios could be captured by FE simulation.

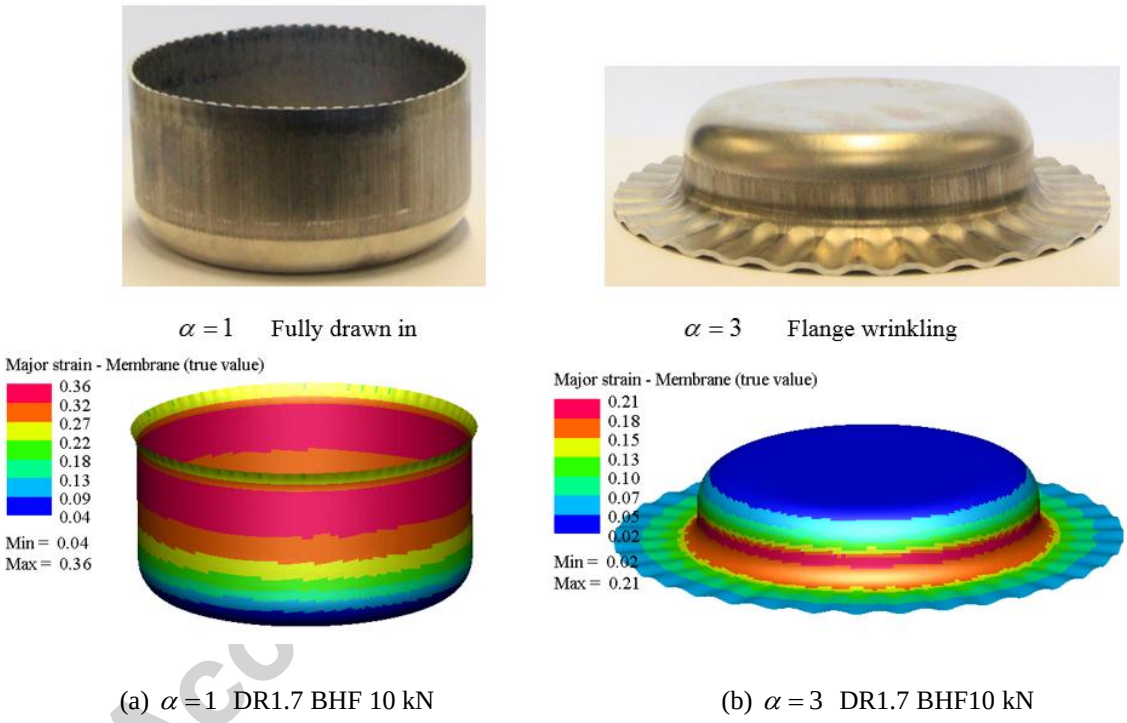

Fig.4. Geometry comparisons of experimental and numerical results using different tool designs: (a) $\alpha = 1$ and (b) $\alpha = 3$

With regard to the material deformation, taking a radial section along the rolling direction, for consistency of experiments, and selecting the central point of bottom surface as the origin as shown in Fig.5 (a), the normalized thickness distributions (t / t_0) defined by Eq. (3) of experimental and computed results are compared at measured points spaced with 5 mm intervals.

$$\hat{t} = t / t_0 \tag{3}$$

Where t is formed thickness and t_0 is original thickness

Fig. 5 (b) shows the normalized thickness distributions of formed parts under different blank-holding forces, 10 kN and 40 kN, for the non-textured blankholder ($\alpha = 0$) and draw ratio 1.7. Fig. 5 (c) shows the normalized thickness distributions of formed parts with blankholder textures: $\alpha = 1$ and $\alpha = 0$ under a blank-holding force of 10 kN and draw ratio 1.8. The symbols indicate measured experimental normalized thickness and the solid lines indicate computed normalized thickness at corresponding positions. Good agreement can be seen between experimental data and computed data. Thinning is captured at the punch radius and the transition point between punch corner radius and cup side-wall as shown in Fig. 5 (a). Hence, it is assumed that the FE model developed in this paper can be used to predict and investigate material deformation and the occurrence of flange wrinkling in the deep drawing processes using macro-textured blankholders.

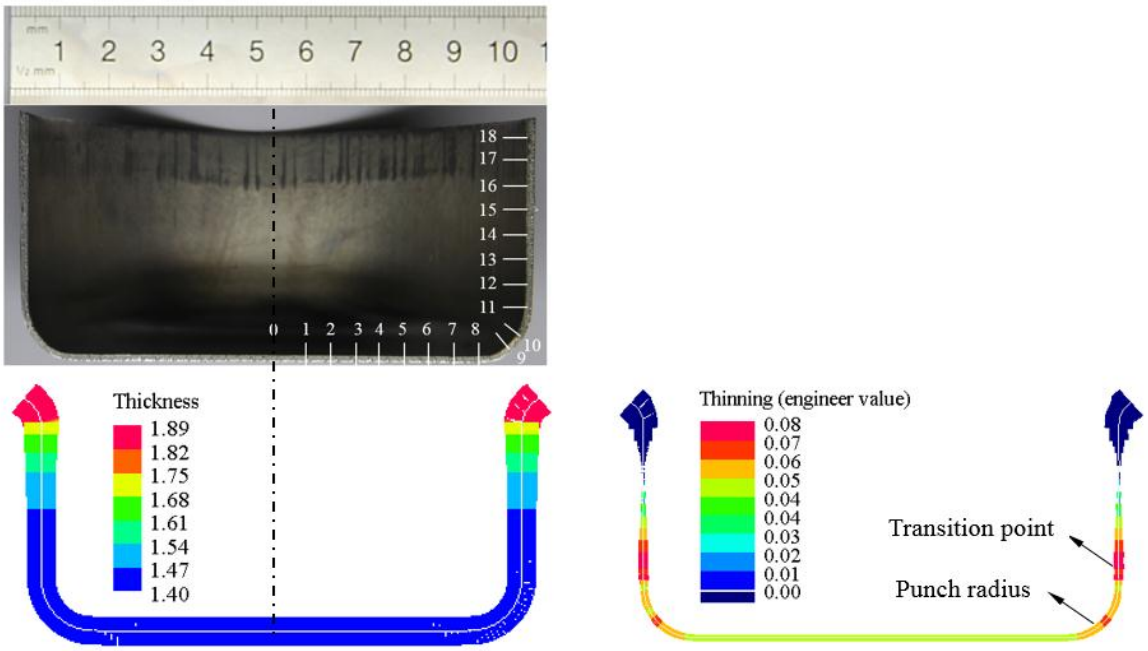

(a) Sectioned profile of formed component and simulation results

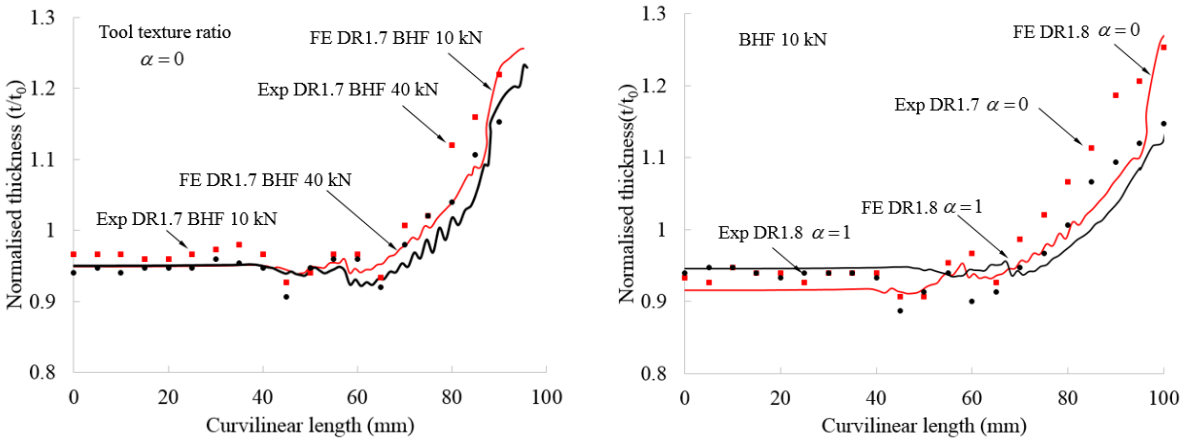

(b) Different blank-holding forces: 10 kN and 40 kN (c) Different tool designs: $\alpha = 1$ and $\alpha = 0$

Fig.5. Comparison of experimental (data points) and computed (solid curves) normalized thickness variations under different forming parameters. DR = drawing ratio and BHF = blank holding force

3.3 Wrinkling occurrence definition

Fig. 6 gives the definition of the occurrence of wrinkling phenomenon, for a particular deflection of the material between two adjacent texture surfaces. When the height between the top point and the bottom point of this deflection (wrinkling wave) reaches 0.1 mm, it defines the onset of wrinkling. This critical condition can be captured accurately by FE simulation, while there might exist some error for experimental results due to the difficulty in precise stroke control of ram and measurement errors. In this figure, b is the initial blank radius and r^* is the instant blank radius when wrinkling occurs.

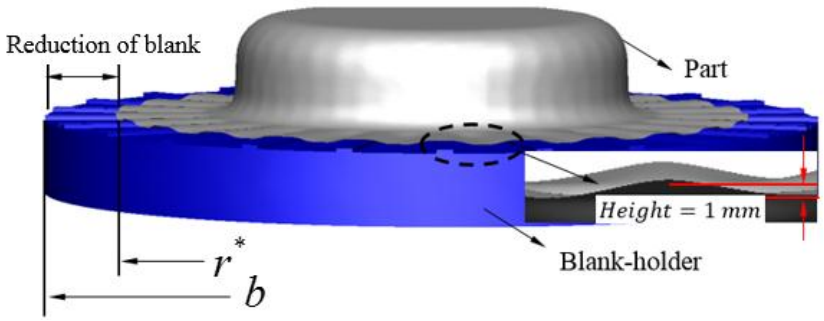

Fig.6. Definition of wrinkling occurrence

4. Analytical buckling model

For flat blankholder surfaces, flange material undergoes a radial tensile stress and a compressive hoop stress during the deep drawing process, and the resulting compressive hoop stress may cause flange area buckling to occur when the blank-holding forces are insufficient. Using macro-texture blankholders material in the flange region can be divided into two zones, as shown in Fig.7, where one zone refers to material constrained by the two tool surfaces and the other group refers to material located in a groove. For simplicity, the constrained material between die and macro-texture surface is defined as Zone ***S***, while the material in the groove is defined as Zone ***G***. As Zone ***G*** material has no blank-holding force constraint, when the test-piece is drawn into the die, the compressive hoop stress may cause Zone ***G*** material to wrinkle. The geometry of this material will vary depending on the blankholder macro-texture geometry and draw ratio. Hence two geometry assumptions are investigated in this section. Zone ***G*** material can be assumed to be a series of discrete one-dimensional beams in each groove or a part of two-dimensional plate in each groove. Two analytical buckling models based these assumptions have been established.

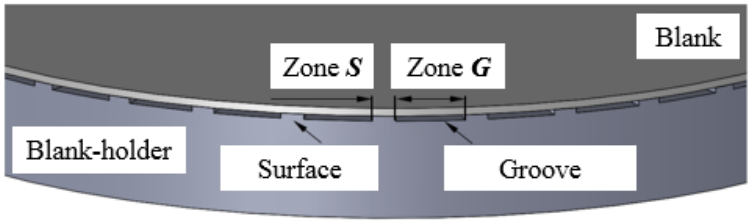

Fig.7. Schematic diagram of test-piece zoning using macro-texture tool

4.1 Mechanics analysis and boundary conditions

For a given tool texture ratio and draw ratio, this material may buckle when the end load (compressive stresses on Zone ***G*** at interfaces between Zone ***S*** and Zone ***G*** material) reaches a certain magnitude. Selecting an infinitesimal unit of material at the interface between Zone ***S*** and Zone ***G***, the stress state of this unit is given in Fig. 8. As Zone ***G*** material has no friction force in the radial direction due to the material being positioned in the groove, it is more likely than the surface constrained material to be drawn into the die, hence, an additional shear stress could be generated at the interface between two neighbouring units. Establishing a force equilibrium equation in the radial direction can be expressed as in Eq. (4).

$$\sigma_r \cdot rd\theta \cdot t + \tau dr \cdot t \sin d\frac{\theta}{2} = (\sigma_r + d\sigma_r)(r + dr)td\theta + 2\mu PS$$
$$+(\tau + d\tau)dr \cdot t \sin d\frac{\theta}{2} + 2|\sigma_\theta| dr \cdot t \sin d\frac{\theta}{2} \quad (4)$$

Where σ_r is the radial tensile stress, τ is the additional shear stress at the interface, σ_θ is the hoop compressive stress, r is the instant radius, θ is the subtended arc angle of this unit, t is test-piece thickness, μ is friction coefficient, S is the unit area calculated using Eq. (5), and P is blank-holding pressure.

$$S = \frac{1}{2}(r + dr)^2 d\theta - \frac{1}{2}r^2 d\theta \quad (5)$$

Applying Tresca yielding criterion $\sigma_r - \sigma_\theta = \sigma_f$ into Eq. (4), where σ_f is material flow stress, and integrating, the radial tensile stress and hoop compressive stress can be obtained as in Eq. (6) and Eq. (7).

$$\sigma_r = \sigma_f \ln\frac{b}{r} + \frac{2\mu P(b-r)}{t} \quad (6)$$

$$\sigma_\theta = \sigma_f (\ln\frac{b}{r} - 1) + \frac{2\mu P(b-r)}{t} \quad (7)$$

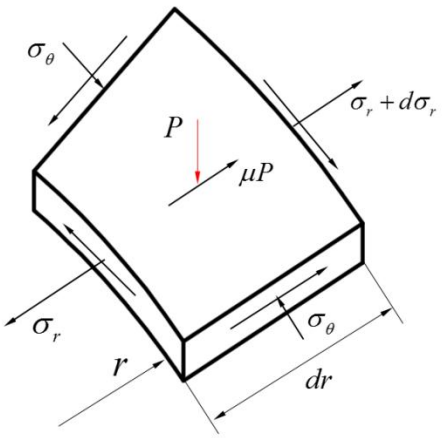

Fig.8. Stress state of an infinitesimal unit at the interface between Zone ***S*** and ***G***

Considering the boundary condition assumption of the constraint of Zone ***G*** material, it is assumed that each Zone ***G*** material is constraint by two half surfaces at two ends.

Establishing a cross-section A-A, from the side view of this cross-section as shown in Fig. 9 (a), schematic diagrams of the hinged and built-in boundary conditions [29] are illustrated in Fig. 9 (b). Each Zone ***G*** material between two surfaces can be regarded as a piece of material constraint by half of the surfaces at two ends.

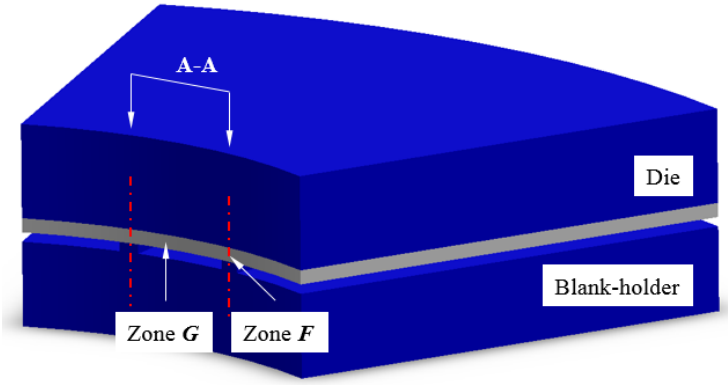

(a) Schematic diagram of boundary condition determination

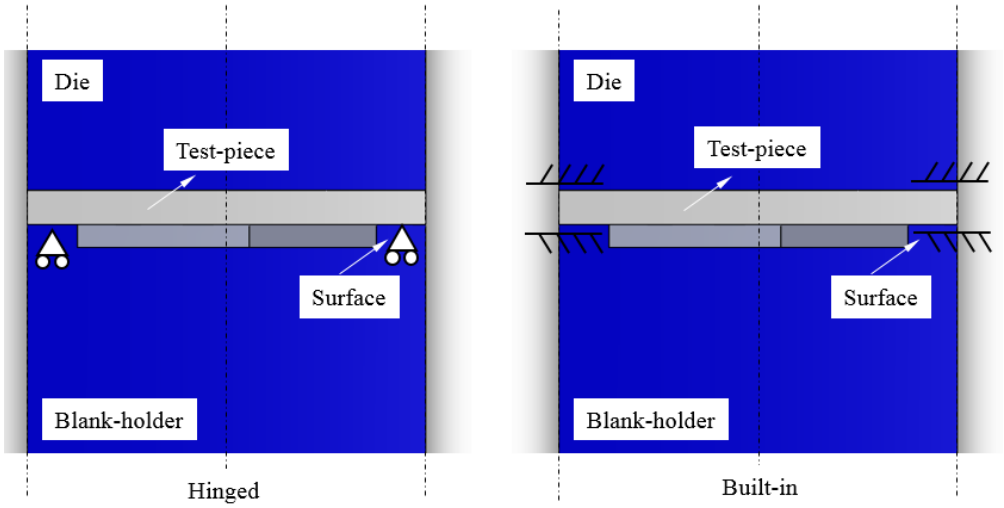

(b) Schematic diagram of hinged and built-in boundary conditions

Fig.9. The boundary condition assumptions using macro-texture tool

4.2 One-dimensional (1-D) buckling model

Applying the one-dimensional beam assumption, when the hoop compressive stress reaches a certain magnitude for a given texture ratio and draw ratio, Zone ***G*** material may buckle via the classic beam buckling phenomenon under the influence of hoop compressive stress as shown in Fig.10. Establishing a Cartesian coordinate system for the analysed Zone ***G*** material, the *X*-axis represents Zone ***G*** material length, the length changes across the width of the beam

f, where $f = r - a$, r is the instant radius of outer flange and a is the radius of inner flange. F^* is the inner force on a particular cross-section, while the *Y*-axis represents the buckling direction.

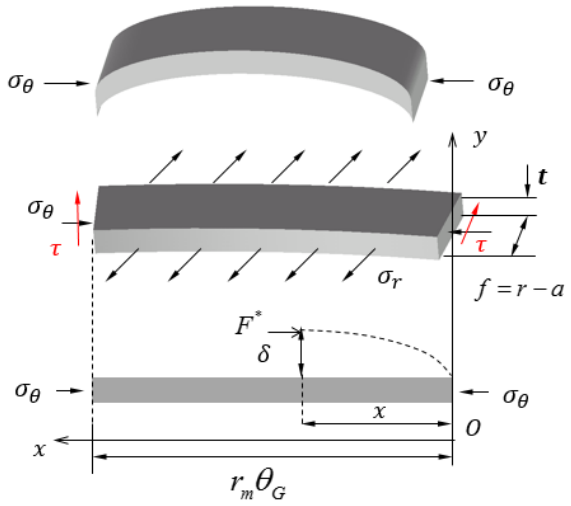

Fig.10. Schematic diagrams of the buckling phenomenon of Zone ***G***

A classic energy method (Senior's method [16]) is applied to analyse the onset of beam buckling. To apply energy method, the deflection expression of wrinkling curve $y(x)$ needs to be obtained first, for the above two boundary conditions, Eq. (8) and (9) need to be satisfied for hinged and built-in boundary conditions respectively. When $x = 0$ and $x = r_m\theta_G$:

$$\begin{aligned} y(x) &= 0 \\ y''(x) &= 0 \end{aligned} \tag{8}$$

$$\begin{aligned} y(x) &= 0 \\ y'(x) &= 0 \end{aligned} \tag{9}$$

The corresponding mathematical expressions of wrinkling deflection can be obtained in (10) and (11).

$$y = \delta \sin \frac{\pi x}{l} \tag{10}$$

$$y = \delta \left(\cos \frac{2\pi x}{l} - 1 \right) \tag{11}$$

Where δ represents the deflection amplitude, l represents the length of a half-wave segment in Eq. (12) and n represents the waving number. r_m is the instant radius of central line of Zone ***G*** material expressed in Eq. (13).

$$l = \frac{\theta_G r_m}{2n} \tag{12}$$

$$r_m = \frac{a+r}{2} \tag{13}$$

Here, reviewing Senior's Euler energy method to calculate this buckling model, the energy used to balance the work done (ΔT) by external force (compressive hoop stress) can be divided into the lateral elastic bending energy E_B and the remaining energy E_p derived from tool clamping between punch and die. Hence, the limit buckling occurrence condition [16] is:

$$\Delta T = E_B + E_p \tag{14}$$

E_B of a half-wave segment of deflection is [16]:

$$E_B = \frac{1}{2}\int_0^l EI(\frac{d^2y}{dx^2})^2 \tag{15}$$

Where E represents Young's modulus and I is the second moment inertia $I = \frac{ft^3}{12}$. In order to reflect the buckling behaviour in the plastic range, a simple assumption proposed by Von Karman [30] is applied, where a reduced modulus E_0 is used to reflect the condition when material is beyond the elastic limit:

$$E_0 = \frac{4EE_t}{(\sqrt{E}+\sqrt{E_t})^2} \tag{16}$$

Where E_t is the material tangent modulus. For the hinged boundary condition, substituting Eq. (10) and Eq. (16) into (15), the expression of E_B can be written as:

$$E_B = \frac{2n^3 E_0 I \delta^2 \pi^4}{\theta_G^3 r_m^3} \tag{17}$$

The work done by hoop compressive external load can be obtained as:

$$\Delta T = \sigma_\theta ft \cdot \lambda \tag{18}$$

Where λ represents the movement of load during bending [16]:

$$\lambda = \frac{1}{2}\int_0^l (\frac{dy}{dx})^2 dx \tag{19}$$

Combining Eq. (10) and Eq. (19) and substituting into Eq. (18), the work done can be expressed as:

$$\Delta T = \sigma_\theta ft \frac{n\delta^2\pi^2}{2\theta_G r_m} \tag{20}$$

The calculation of E_P incorporating Senior's lower limit methods [16] is written in Eq. (21).

$$E_P = \int_0^l \int_o^y fqdydx \tag{21}$$

Where q simulates the tool clamping of the inner flange periphery. Morley [31] found that the deflection at the mean radius is proportional to the load:

$$y = \frac{Cqf^5}{8E_0 I} \tag{22}$$

For Senior's lower limit, the deflection is proportional to the buckling wave amplitude [16]:

$$q = Ky \tag{23}$$

Then E_P of lower limit can be obtained using Eqs. (10), (21), (22) and (23):

$$E_P = \frac{fK\delta^2\theta_G r_m}{8n} \tag{24}$$

Recalling the critical condition of occurrence of wrinkling in Eq. (14), and substituting Eqs. (7), (12), (13), (17), (20) and (24) into (14), the onset condition of plastic buckling using hinged boundary condition can be written as:

$$\frac{\sigma_f \ln\frac{b}{r} + \frac{2\mu P(b-r)}{t}}{E_0} - \left(\frac{t}{f}\right)^2 \cdot \left(\frac{4\pi^2 n^2 (r-a)^2}{3\theta_G^2 (r+a)^2} + \frac{\theta_G^2 (r+a)^2}{24(r-a)^2 n^2 \pi^2}\right) = 0 \tag{25}$$

In a similar way, the onset condition of plastic buckling using built-in boundary condition can be written as:

$$\frac{\sigma_f \ln\frac{b}{r}+\frac{2\mu P(b-r)}{t}}{E_0}-\left(\frac{t}{f}\right)^2\cdot\left(\frac{64\pi^2n^2(r-a)^2}{3\theta_G^2(r+a)^2}+\frac{5\theta_G^2(r+a)^2}{24(r-a)^2n^2\pi^2}\right)=0 \qquad (26)$$

4.3 Two-dimensional (2-D) buckling model

An additional means of analysing buckling for this geometry is to consider all the material in Zone ***G*** as part of a 2-D plate and express mathematical equations in the form of a cylindrical coordinate system on the annular flange surface. To this end, Yu et al. has established the mathematical expression of deflection [18] for two-dimensional buckling based on the energy method, where the radial coordinate is considered, then the mathematical expression of deflection is $\delta(r-a)f(\theta)$. For the use of macro-textured blankholders, boundary conditions in the hoop direction must be applied which can be assumed as either hinged (27) or built-in (28) respectively. Hence, the boundary conditions at $\theta=0$ and $\theta=\theta_G$ for the hinged and built-in case are expressed as:

$$\begin{aligned} f(\theta)&=0\\ f''(\theta)&=0 \end{aligned} \qquad (27)$$

$$\begin{aligned} f(\theta)&=0\\ f'(\theta)&=0 \end{aligned} \qquad (28)$$

Hence, the deflection curve of the wrinkles can be mathematically expressed using Eq. (29) and (30) for hinged and built-in boundary conditions respectively.

$$w(r,\theta)=\delta(r-a)\sin(\frac{n\pi\theta}{\theta_G}) \qquad (29)$$

$$w(r,\theta)=\delta(r-a)\cos(\frac{2n\pi\theta}{\theta_G}-1) \qquad (30)$$

Where δ is the wave amplitude.

In this paper, only plastic buckling has been investigated due to the large draw ratio and thin sheet used for this deep drawing process. Hence, the reduced Young's modulus is still applied to reflect the condition when material is beyond the elastic limit. Applying the energy method to conduct the instability criterion for Zone ***G*** material, the strain energy of plastic bending can be calculated using Eq. (31) [33] for Cartesian coordinate system and is transformed to Eq. (32) for a cylindrical coordinate system.

$$\Delta U^P = \int_a^r \int_0^{\theta_G} \frac{D^P}{2} \left\{ (\frac{\partial^2 w}{\partial x^2} + \frac{\partial^2 w}{\partial y^2})^2 - 2(1-\nu) \left[\frac{\partial^2 w}{\partial x^2} \frac{\partial^2 w}{\partial y^2} - (\frac{\partial^2 w}{\partial x \partial y})^2 \right] \right\} dxdy \tag{31}$$

$$\begin{aligned} \Delta U^P = \int_a^r \int_0^{\theta_G} [& \frac{D^P}{2} (\frac{\partial^2 w}{\partial r^2} + \frac{1}{r}\frac{\partial w}{\partial r} + \frac{1}{r^2}\frac{\partial^2 w}{\partial \theta^2})^2 - D^P(1-\nu)\frac{\partial^2 w}{\partial r^2}(\frac{1}{r}\frac{\partial w}{\partial r} + \frac{1}{r^2}\frac{\partial^2 w}{\partial \theta^2}) \\ & + D^P(1-\nu)(\frac{1}{r}\frac{\partial^2 w}{\partial r \partial \theta} - \frac{1}{r^2}\frac{\partial w}{\partial \theta})^2] r dr d\theta \end{aligned} \tag{32}$$

Where θ_G is defined as the subtended arc angle of the 2-D plate suitable for different tool textures and ν is the Poisson's ratio. A radius ratio ρ is defined as shown in Eq. (33). D^P represents the bending rigidity of test-piece in Eq. (34).

$$\rho = a / r \tag{33}$$

$$D^P = \frac{E_0 t^3}{12(1-\nu^2)} \tag{34}$$

For the hinged boundary condition, substituting Eqs. (29), (33) and (34) into (32), the strain energy of bending can be calculated to obtain the expression in Eq. (35).

$$\Delta U^P_{Hinged} = D^P \delta^2 F^P_{Hinged}(\nu, \rho, \theta_G, n) \tag{35}$$

In terms of the work done by external forces, the expression of work [33] is given in Eq. (36).

$$\Delta T^P = -\frac{1}{2} \iint \left\{ \sigma_r t (\frac{\partial w}{\partial r})^2 + \sigma_\theta t (\frac{1}{r}\frac{\partial w}{\partial \theta})^2 \right\} r dr d\theta \tag{36}$$

For plastic buckling analysis of Zone ***G*** on the annular flange area, the radial and hoop stresses can be calculated using the Tresca yielding criterion. In order to simplify the mathematical integration in Eq. (36), blank-holding force is neglected and thus radial and hoop stresses in Eqs. (6) and (7) can be simplified to Eqs. (37) and (38).

$$\sigma_r = \sigma_f \ln(b / r) \tag{37}$$

$$\sigma_\theta = \sigma_f [\ln(b / r) - 1] \tag{38}$$

Substituting (29), (34) and (38) into (36), the work done is expressed as:

$$\Delta T^P_{Hinged} = \sigma_f \delta^2 H^P_{Hinged}(t, r, \rho, \theta_G, n) \tag{39}$$

The onset condition of plastic buckling of Zone ***G*** material using the hinged boundary condition at the annular flange area can be expressed as:

$$\Delta U^{P}_{Hinged} = \Delta T^{P}_{Hinged} \tag{40}$$

In a similar way, the onset condition using the built-in boundary condition can be expressed as (41):

$$\Delta U^{P}_{Built-in} = \Delta T^{P}_{Built-in} \tag{41}$$

The onset conditions of plastic buckling of zone ***G*** material can be written as (42) and (43) for the hinged and built-in boundary conditions respectively:

$$\frac{\sigma_f}{E_0} - \frac{F^{P}_{Hinged}(\nu, \rho, \theta_G, n)}{H^{P}_{Hinged}(t, r, \rho, \theta_G, n)} = 0 \tag{42}$$

$$\frac{\sigma_f}{E_0} - \frac{F^{P}_{Built-in}(\nu, \rho, \theta_G, n)}{H^{P}_{Built-in}(t, r, \rho, \theta_G, n)} = 0 \tag{43}$$

4.4 CDM material model

Considering the above two analytical buckling models, the onset of buckling is determined by both material strength σ_f / E_0 and geometry parameters of Zone ***G*** material. Due to the flow stress and reduced Young's modulus of Zone ***G*** material that varies with the degree of deformation, the establishment of corresponding relationships between geometry parameter and material constitutive equations is necessary.

Firstly, the stress strain behaviour of the alloy needs to be modelled. A novel continuum damage based material model proposed by Lin et al. [34] is applied here to model constitutive equations of AA6082-O condition at room temperature. The list of equations is given below. This series of multi-axial dislocation based constitutive equations can be converted to uniaxial constitutive equations via adjusting material constants in the equations.

$$\dot{\varepsilon}_p = \left(\frac{\sigma_e / (1-\omega) - R - k}{K} \right)^{n_1} \tag{44}$$

$$\dot{\varepsilon}^{p}_{ij} = \frac{3}{2} \frac{S_{ij}}{\sigma_e} \dot{\varepsilon}^{p}_{e} \tag{45}$$

$$\dot{R} = 0.5B\bar{\rho}^{-0.5}\dot{\bar{\rho}} \tag{46}$$

$$\dot{\bar{\rho}} = A(1-\bar{\rho})\left|\dot{\varepsilon}_p\right| - C\bar{\rho}^{n_2} \tag{47}$$

$$\sigma_{ij} = (1-\omega)D_{ijkl}(\varepsilon_{kl} - \varepsilon_{kl}^p) \tag{48}$$

$$\dot{\omega} = \frac{\Delta}{(\alpha_1+\alpha_2+\alpha_3)^{\varphi}}\left\langle \frac{\alpha_1\sigma_1 + 3\alpha_2\sigma_H + \alpha_3\sigma_e}{\sigma_e}\right\rangle^{\varphi} \frac{\eta_1\sigma_e}{(1-\omega)^{\eta_3}}(\dot{\varepsilon}_p)^{\eta_2} \tag{49}$$

Eq. (45) represents the effective plastic strain rate $\dot{\varepsilon}_p$, where $\sigma_e = (3S_{ij}\cdot S_{ij})/2^{1/2}$ is effective stress, $S_{ij} = \sigma_{ij} - \delta_{ij}\sigma_{kk}/3$ is the deviatoric stress tensor, k is the initial yield stress, ω is the damage factor, K and n are material constants. Eq. (45) gives the expression of plastic strain rate tensor to model multi-axial power-law visco-plastic behaviour. The evolution of material hardening, $\dot{R}$, is given by Eq. (46), which is a function of the normalized dislocation density, $\bar{\rho} = (\rho - \rho_i)/\rho_m$, ρ_i is the dislocation density for the initial material and ρ_m is the maximum (saturated) dislocation density. Hence $\bar{\rho}$ varies from 0 (the initial state) to 1 (the saturated state). Eq. (47) gives the evolution of dislocation density, $\bar{\rho}$, where A and C are material constants. A detailed explanation of this equation is illustrated in Lin et al. [35]. In Eq. (48), σ_{ij} is the stress tensor and D_{ijkl} is the elastic matrix of the material. Eq. (49) represents the multi-axial damage evolution, $\dot{\omega}$, which comes from the uniaxial form of the multi-axial stress-state effect. Where α_1 , α_2 and α_3 are weighting parameters considering stress state effect on damage evolution, φ is a multi-axial stress damage exponent and Δ is a correction factor related with different strain measurement method, η_1, η_2 and η_3 are material constants. Considering no damage arises in the flange, the damage effect in Eq. (49) can be neglected by setting Δ , φ and η_1 in Table.3, and modelling only the strain hardening stage, as shown in Fig.11 (a), the unbroken line represents the numerical fitting, while the red symbols represent experimental data. Table. 3 gives the needed material constants for Eq. (45) to Eq. (50).

Tab.3. Material constants in CDM material model of AA6082-O condition

K (MPa)	k (MPa)	n_1	B (MPa)	A	C	n_2
9	5.1	9	200	2.15	0	1.8
Δ	φ	η_1	η_2	η_3	E (MPa)	
1	0	0	20	1	70000	

The tangent modulus E_t in (50) and flow stress σ_f can be obtained for different strains.

$$E_t^i = \frac{\sigma^{i+1} - \sigma^i}{\varepsilon^{i+1} - \varepsilon^i} \tag{50}$$

Secondly, when the blank is drawn to a certain position (from r^0 towards r^j) as shown in Fig.11 (b) corresponding to a certain blank diameter reduction, as flange material has plastic deformation strain here, hence, the flow stress and reduced modulus are dependent on the different strain. To find this approximate relationship, assuming the region of Zone ***G*** material as a thin slab which only sustains hoop compressive stress, the deformation type of this slab can be assumed as an uniaxial compression test. Then the instant blank diameter reduction $\Delta^i \approx b - r^i / b$ corresponding to a certain true strain in uniaxial tensile test is calculated as in Eq. (51). Recalling the critical conditions of wrinkling, for a given blank diameter reduction, σ_f / E_0 and geometry functions can be calculated using the instant geometry dimensions and CDM material model. When the left sides equal to zero, wrinkling occurs. Combining the CDM material model with the critical conditions of wrinkling occurrence in Eqs. (25), (26), (42) and (43), analytical buckling models for a given material with different process parameters and tool designs can be obtained. Considering the surface constraint of Zone ***G*** material using macro-textured blankholder, each Zone ***G*** material is constrained by two half surfaces as shown in Fig. 9. Assuming each unit (one Zone ***G*** and two half surfaces) has a wave when buckling occurs, then *n* value can be determined for different texture ratios in Eq. (52). Table. 4 gives the remaining necessary process parameters of analytical buckling models

$$\varepsilon_i = \ln(1 + \Delta_i) \tag{51}$$

$$n = \frac{\theta_G}{(\theta_G + \theta_S)} \tag{52}$$

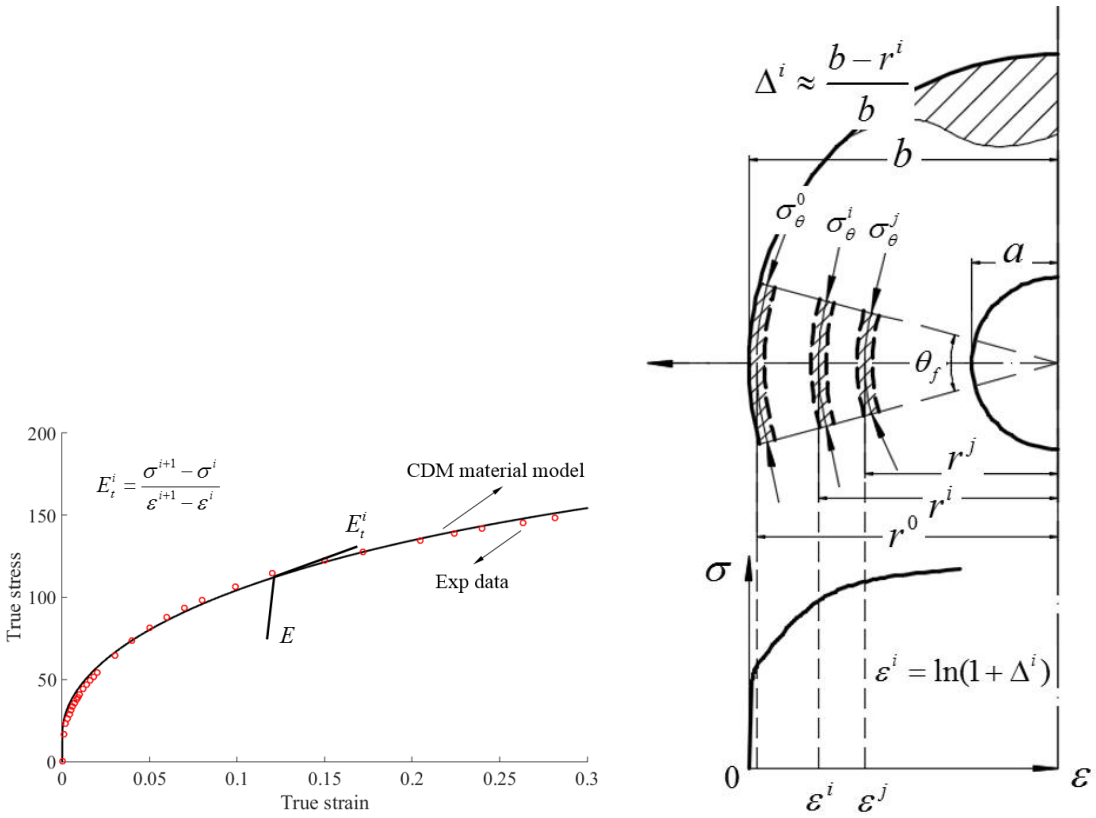

(a) Material model fitting (b) Corresponding relationship

Fig.11. Material fitting and corresponding relationships in buckling models

Tab.4. The remaining process parameter

a	ν	Friction coefficient	θ_G (°)	θ_s (°)	Draw ratio
61.65	0.33	0.1	2.5, 7.5 and 12.5	2.5	1.7,1.8 and 1.9

5. Results and Discussions

5.1 Blank-holding force effect

Fig. 12 illustrates the effect of blank-holding force on the occurrence of wrinkling with tool textures: $\alpha = 3$ and $\alpha = 5$ at blank-holding forces (BHF) of 10 kN and 40 kN for draw ratios 1.7, 1.8 and 1.9 respectively. The forming speed for all tests was 75 mm/s. The solid symbols in the figure represent experimental data of wrinkling occurrence: 10 kN (red) and 40 kN (black). 1-D beam buckling model with a hinged boundary condition was applied here to investigate the blank-holding force effect. Combining the equations (25), (50), (51) and material model equations together, the analytical wrinkling onset points of different tooling and test conditions could be obtained and plotted using Matlab as shown in the four lines of Fig.12. The dash and solid lines represent the tool texture design $\alpha = 3$ and $\alpha = 5$ with blank-holding forces 10 kN for the red and 40 kN for the black. Wrinkling occurrence could thus be analysed and compared experimentally and analytically. It can be seen that there is little difference in analytical lines for BHF 10 kN and BHF 40 kN. Little differences between BHF 10 kN and 40 kN cases can be still observed in the experimental results. It should also be noted that wrinkling begins on one end, then the outer flange material buckles which leads to wrinkling spreading inwards in the radial direction. Furthermore, the experimental and analytical results also have similar variation trends, which shows that blank-holding force has no clear effect on the wrinkling occurrence. The reason is that, recalling Eq. (7), before wrinkling occurs (small diameter reduction), compared with the material deformation load (first item on the right), the blank-holding force effect (second item on the right) on hoop compressive stress is much smaller and can be neglected. This phenomenon further certifies that the approximations for Eq. (37) and Eq. (38), where the blank-holding force terms in equations for two-dimensional buckling model are eliminated, is reasonable.

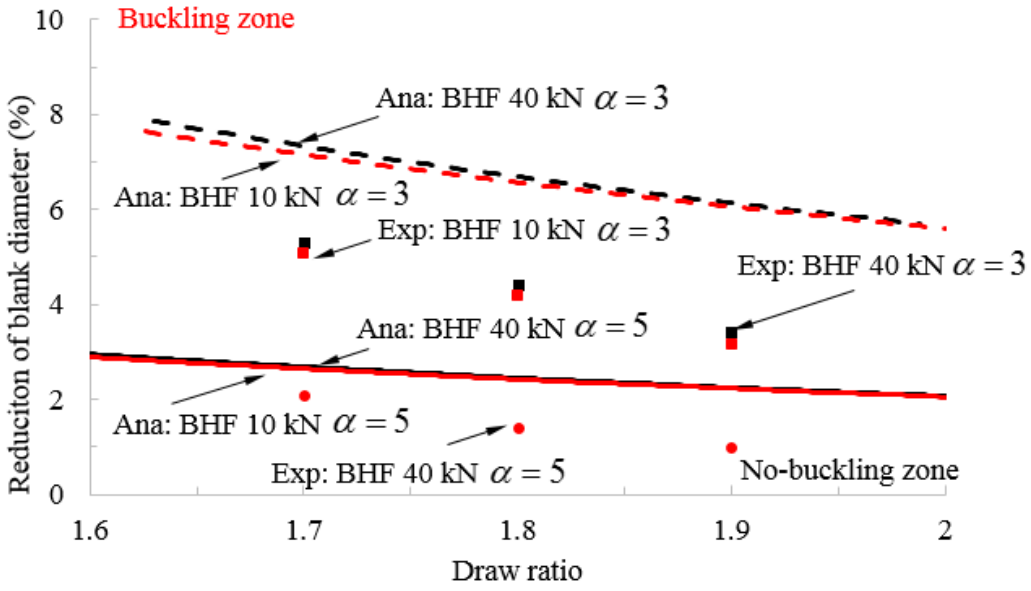

Fig.12. Blank-holding force effects on wrinkling occurrence, where lines represent analytical results, solid symbols represent experimental results.

5.2 Boundary condition effect

Recalling Eqs. (25), (26), (42) and (43), two kinds of boundary conditions, hinged and built-in are both investigated. Fig. 13 shows the comparison of analytical results using 1-D (red) and 2-D (black) buckling models with a tool texture design $\alpha = 5$, where the solid lines represent the hinged boundary condition and the dash line represents the built-in boundary condition. Corresponding experimental results (red) and numerical results (black) are given and compared with analytical lines. Less differences between experimental and analytical results are found using the hinged boundary condition, while using built-in boundary condition, the analytical line is much higher than using the hinged boundary condition, which means that wrinkling phenomena occurs at a greater blank diameter reduction. Due to this large difference between analytical results (built-in) and experimental, numerical results, hence the assumption of built-in boundary condition of Zone ***G*** material is not as accurate as the hinged boundary condition to reflect the surface constraints of the Zone ***G*** material. In addition, 2-D buckling analytical model has a better agreement with the experimental and numerical results than 1-D beam buckling analytical model for the tool design $\alpha = 5$, which

illustrates that 2-D plate buckling is more accurate to reflect the geometry character of Zone ***G*** material, detailed explanations are given in Section 5.3 and 5.4.

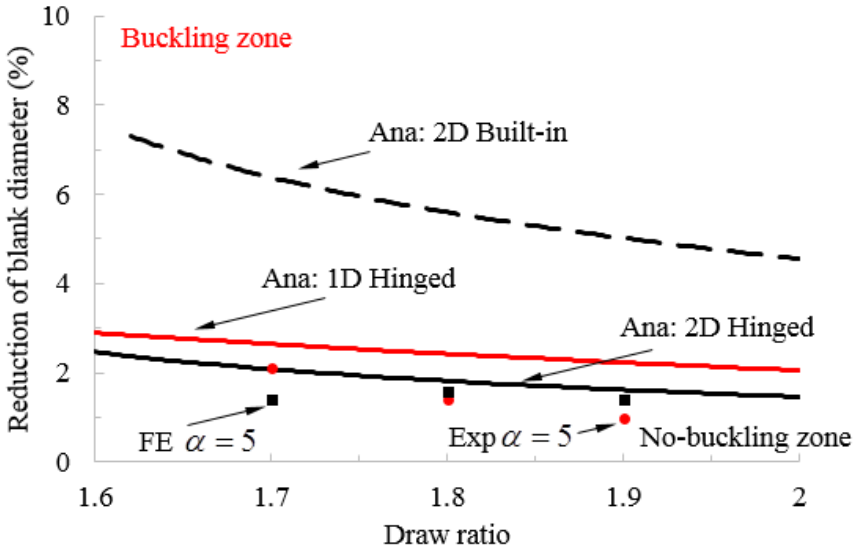

Fig.13. Boundary condition effects on wrinkling occurrence, where solid lines represent the hinged boundary condition and dash lines represents the built-in boundary condition.

5.3 Texture ratio effect

Fig. 14 shows the texture ratio effect on wrinkling occurrence for 1-D (solid line) and 2-D (dashed line) analytical curves at a blank-holding force 10 kN and forming speed 75 mm/s. Typical experimental results (solid symbols) are also presented. The regions below the two analytical curves represent no buckling zones, while the regions above represent buckling zones. With the increase of texture ratio, wrinkling occurs more readily and the limit reduction of diameter decreases. As shown in Fig. 14, if the texture ratio is small enough (Fig. 14 No.1 for $\alpha = 1$), the test-piece can be fully drawn without wrinkling, while if the texture ratio is greater, wrinkling is generated when the test-piece is drawn with a certain diameter reduction (Fig.14 No.3 for $\alpha = 3$). Hence, a process window for the onset of wrinkling can be constructed. Three typical experimental test conditions were used to validate the analytical models. For Test No.1 with a texture ratio $\alpha = 1$ and draw ratio 1.8, a fully drawn cup could be formed; For Test No.2 with a texture ratio $\alpha = 3$ and draw ratio 1.8, the experimental point is located in the region between two analytical buckling models. The 1-D model curve is higher than 2-D curve, this might be because for the two-dimensional plate assumption, the

Zone ***G*** material is more likely to experience wrinkling compared with the one-dimensional beam. For Test No.3, the experimental point representing a formed part with severe wrinkling, is located above these two analytical curves. The experimental results indicate the 2-D plate assumption buckling model represents wrinkling behaviour with useful accuracy. For a certain process draw-ratio and test-piece material, there exists a limit texture ratio. If the tool texture ratio is lower than this limit magnitude, no wrinkling occurs. For a particular tool texture ratio wrinkling can be avoided by limiting the magnitude of the flange diameter reduction.

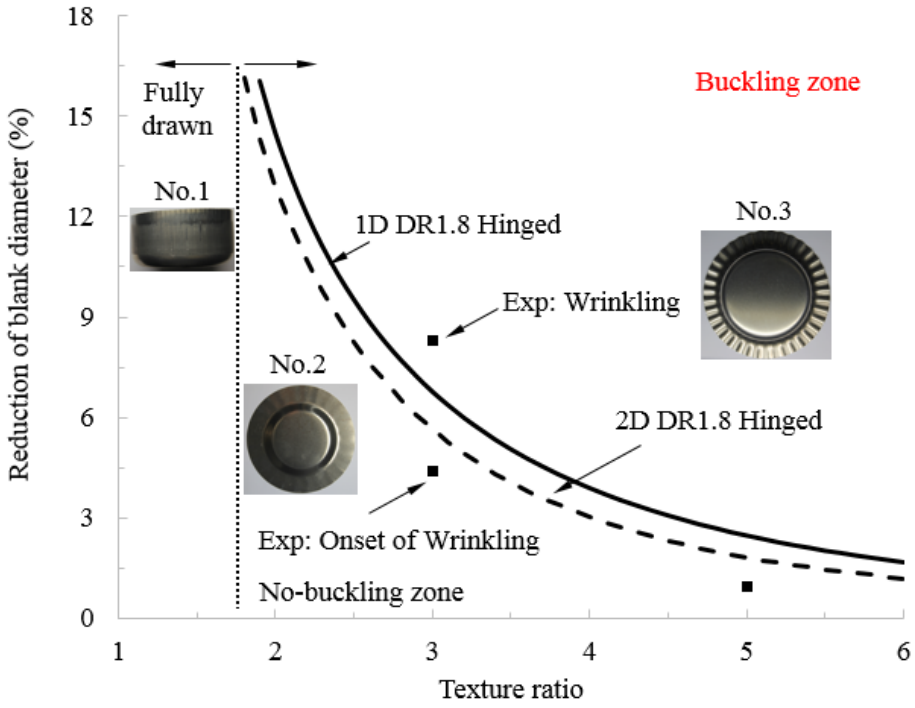

Fig.14. Texture ratio effects on wrinkling occurrence, where solid line represents 1-D analytical result and dashed line represents 2-D analytical result; symbols represent experimental results

5.4 Draw ratio effect

Test-piece draw ratio is another factor affecting the occurrence of wrinkling. This is because both texture ratio and draw ratio have coupled effects on controlling Zone ***G*** material geometry. Fig. 15 shows the draw ratio effect on wrinkling occurrence for blankholder textures: $\alpha = 3$ and $\alpha = 5$, at a blank-holding force 10 kN and forming speed 75 mm/s. From the analytical curves, experimental and numerical results, it can be seen that, with the increasing of draw ratio, wrinkling is more likely to occur. This is due to the larger initial work-piece diameter resulting in more material with no blank-holding force constraint, and

the increased free Zone ***G*** material area will be more likely to experience buckling. In addition, for 1-D analytical buckling model the error between experimental results and analytical results for $\alpha = 5$ is greater than those of $\alpha = 3$, this difference becomes greater as well with the increasing of draw ratio for $\alpha = 5$. The reason for this might be that, for a greater texture ratio, 1-D beam assumption is not accurate to reflect the geometry feature of Zone ***G*** material, the reason is that, with the increasing of draw ratio or texture ratio, the geometry shape of Zone ***G*** material is more like of a part of plate due to the dimension difference between arc length and thickness becomes large.

For a greater texture ratio, the onset of wrinkling occurs at a smaller blank diameter reduction and combined with the imperfect circle of the flange due to anisotropy, results in measurements being difficult to record. Furthermore, the increasing of thickness is ignored by assuming initial thickness is constant which contributes to simplifying the calculation significantly. For a given texture ratio $\alpha = 5$, the difference between analytical and experimental, numerical results for the 2-D analytical model are lower than those of the 1-D analytical model. In addition, with the increase of draw ratio, the critical blank diameter reduction when wrinkling occurs is smaller, which illustrates that a larger draw ratio may allow wrinkling to occur more easily, this trend is similar with the texture ratio effect.

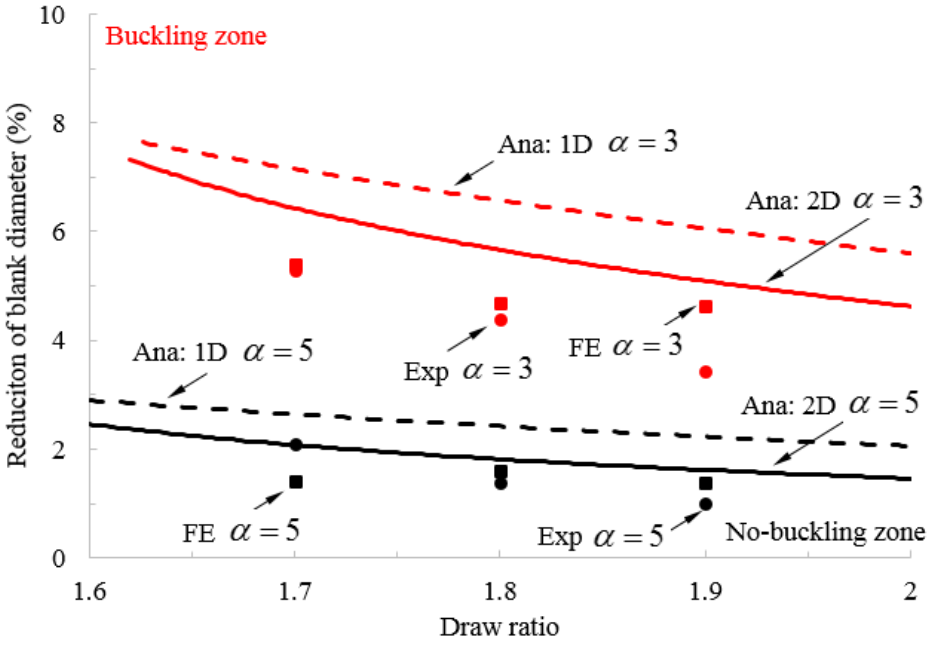

Fig.15. Draw ratio effects on wrinkling occurrence at a blank-holding force 10 kN and forming speed 75 mm/s.

6. Conclusions

The work described in this paper is an investigation of the occurrence of wrinkling in the flange of deep drawn cylindrical cups in aluminium alloy using macro-textured blank-holder surfaces, through experimental, numerical and analytical methods. The textures comprised radial grooves of rectangular cross-section with the bearing area defined by a ratio of groove to surface areas. With a small texture ratio $\alpha = 1$, the test-piece material could be fully drawn into the die without the occurrence of wrinkling, while using $\alpha = 3$ and $\alpha = 5$, wrinkling occurred when the diameter reduction reached a threshold magnitude.

A finite element model has been established to model the material deformation and wrinkling defects using macro-textured tool surfaces. Close agreement between normalized thickness distributions could be found between experimental and numerical results for different test and tooling conditions.

Two analytical buckling models: 1-D (assumed beam) and 2-D (assumed plate) of aluminium alloy in deep drawing with macro-textured blankholder were established for the first time and validated by both experimental and numerical results. The effect of blank-holding force on the occurrence of wrinkling was investigated using a 1-D analytical model, where this effect was found to be insignificant compared to the effects of texture ratio and draw ratio, with the increase of texture ratio and draw ratio resulting in wrinkling defects being more likely to occur.

It was found that there exists reasonable error between the analytical model and experimental data, due to the geometry assumption of material in the groove of a texture. The 2-D plate buckling model was found to exhibit better agreement with experimental results compared to the 1-D beam plate buckling model. Furthermore, applying the hinged boundary condition surface constraint on Zone ***G*** was found to show more representative results than the built-in boundary condition. These analytical buckling models could provide useful guidelines in designing macro-textured tool surfaces for sheet stamping processes.

7. Acknowledgements

The work described in this paper was supported by the European Commission 7th Framework Programme (Grant agreement no: 604240) as part of the project ‘LoCoLite: An industry system enabling the use of a patented materials processing technology for Low Cost forming of Lightweight structures for transportation industries’. Moreover, the contribution

of cast and machined tools by Plasmaterm SA are greatly appreciated. Furthermore, the authors would like to thank the China Scholarship Council (CSC) for providing a scholarship to K. Zheng.

References

1. Laurent H, Coer J, Manach PY, Olivera MC, Menezes LF. Experimental and numerical studies on the warm deep drawing of an Al-Mg alloy. Int J Mech Sci 2015; 93: 59-72. doi:10.1016/j.ijmecsci.2015.01.009
2. Greze R, Manach PY, Laurent H, Thuillier S, Menezes LF. Influence of the temperature on residual stresses and springback effect in an aluminium alloy. Int J Mech Sci 2010; 52: 1094-1100. doi:10.1016/j.ijmecsci.2010.04.008
3. Chu X, Leotoing L, Guines D, Ragneau E. Temperature and strain rate influence on AA5086 Forming Limit Curves: Experimental results and discussion on the validity of the M-K model. Int J Mech Sci 2014; 78: 27-34. doi:10.1016/j.ijmecsci.2013.11.002
4. Foster AD, Dean TA, Lin J (2013) Process for forming aluminium alloy sheet components, Patent No. EP 2,324,137, January 16.
5. Mohamed MS, Foster AD, Lin J, Balint DS, Dean TA. Investigation of deformation and failure features in hot stamping of AA6082: Experimentation and modelling. Int J Mach Tool Manu 2012; 53(1): 27-38. doi:10.1016/j.ijmachtools.2011.07.005
6. Esmaeili S, Lloyd DJ, Poole WJ. A yield strength model for the Al-Mg-Si-Cu alloy AA6111. Acta Mat 2003; 51(8): 2243-2257. doi:10.1016/S1359-6454(03)00028-4
7. Karbasian H, Tekkaya AE. A review on hot stamping. J Mat Process Tech 2010; 210(15): 2103-2118. doi:10.1016/j.jmatprotec.2010.07.019
8. Merklein M, Lechler J, Stoehr T. Investigations on the thermal behavior of ultra high strength boron manganese steels within hot stamping. Int J Mat Form 2009; 2(1): 259-262. doi:10.1007/s12289-009-0505-x
9. Bosetti P, Bruschi S, Stoehr T, Lechler J, Merklein M. Interlaboratory comparison for heat transfer coefficient identification in hot stamping of high strength steels. Int J Mat Form 2010, 3(1): 817-820. doi: 10.1007/s12289-010-0895-9
10. Ni WY, Cheng YT, Weiner AM, Perry TA. Tribological behavior of diamond-like-carbon (DLC) coatings against aluminum alloys at elecated temperatures. Sur Coat Tech 2006; 201(6): 3229-3234. doi:10.1016/j.surfcoat.2006.06.045
11. Hu TC, Hu LT, Ding Q. Effective solution for the tribological problems of Ti-6Al-4V: Combination of laser surface texturing and solid lubricant film. Surf Coat Tech 2012; 206(24): 5060-5066. doi:10.1016/j.surfcoat.2012.06.014
12. Costa HL, Hutchings IM. Effects of die surface patterning on lubrication in strip drawing. J Mat Process Tech 2009; 209(3): 1175-1180. doi:10.1016/j.jmatprotec.2008.03.026
13. Costa HL, Hutchings IM. Hydrodynamic lubrication of textured steel surfaces under reciprocating sliding conditions. Tribol Int 2007; 40(8): 1227-1238. doi:10.1016/j.triboint.2007.01.014
14. Zheng K, Politis DJ, Lin J, Dean TA. An experimental and numerical investigation of the effect of macro-textured tool surfaces in hot stamping. Int J Mat Form 2015; doi: 10.1007/s12289-015-1273-4
15. Geckeler, J. Plastisches Knicken der Wandung von Hohlzylindern und einige andere Faltungserscheinungen an Schalen und Blechen. ZAMM-Journal of Applied Mathematics and Mechanics/Zeitschrift für Angewandte Mathematik und Mechanik 1928; 8(5): 341-352. doi: 10.1002/zamm.19280080502

16. Senior BW. Flange wrinkling in deep-drawing operations. J Mech and Phy Solids 1956; 4(4): 235-246. doi:10.1016/0022-5096(56)90032-1
17. Kadkhodayan M, Moayyedian F. Analytical elastic-plastic study on flange wrinkling in deep drawing process. Sci Iranica 2012; 18(2): 250-260. doi:10.1016/j.scient.2011.03.020
18. Yu TX, Johnson W. The buckling of annular plates in relation to deep-drawing process. Int J Mech Sci 1982; 24: 175-188. doi:10.1016/0020-7403(82)90036-4
19. Hutchinson JW. Plastic buckling. Adv in App Mech 1974; 67: 14-16. doi:10.1016/S0065-2156(08)70031-0
20. Hutchingson JW, Neale KW. Wrinkling of curved thin sheet metal;. Plas Instability 1985; 71-78.
21. Hill R. A general theory of uniqueness and stability in elastic/plastic solids. J Mech Phy Solids 1958; 6: 2336-249. doi:10.1016/0022-5096(58)90029-2
22. Wang CT, Kinezel G, Altan T. Wrinkling criterion for an anisotropic shell with compound curvtures in sheet forming. Int J Mech Sci 1994; 26(10): 945-960. doi:10.1016/0020-7403(94)90056-6
23. João Pedro de Magalhães Correia, Gérard Ferron. Wrinkling predictions in the deep-drawing process of anisotropic metal sheets. J Mat Process Tech 2004; 218(1-3):178-190. doi:10.1016/j.jmatprotec.2004.04.270
24. Cao J, Karafillis A, Ostrowski M. Prediction of flange wrinkles in deep drawing. Stu in App Mech 1997; 45: 301-310. doi:10.1016/S0922-5382(97)80032-3
25. Cao J. Prediction of plastic wrinkling using the energy method. J Appl Mech 1999; 66(3): 646-652. doi:10.1115/1.2791505
26. Wang XW, Wang Y. Buckling analysis of thin rectangular plates under unaxial or biaxial compressive point loads by the differential quadrature method. Int J Mech Sci 2015; 101-102: 38-48. doi:10.1016/j.ijmecsci.2015.07.021
27. Smith Metals (2015) Aluminium Data Sheets. http://www.smithmetal.com/downloads/aluminium_datasheets.htm. Accessed 28 September 2015.
28. Aginagalde A, Gomez X, Galdos L, Garcia C. Heat treatment selection and forming strategies for 6082 aluminum alloy. J Eng Mat Tech 2009; 131(4): 044501. doi:10.1115/1.3120384
29. Timoshenko, SP, Gere JM, and Prager W. Theory of elastic stability. Jour of App Mech 1962; 29 (1): 220. doi:10.1115/1.3636481
30. Timoshhenko SP, Goodier JN. Theory of elasticity 2nd ed. New York: McGraw-Hill; 1951.
31. Morley A. Strength of materials 8th ed, Green: Longmans; 1934
32. Chu E, Xu Y. An elastoplastic analysis of flange wrinkling in deep drawing process. Int J Mech Sci 2001; 43(6): 1421-1440. doi:10.1016/S0020-7403(00)00091-6
33. Timoshenko SP, Woinowsky-Krieger S. Theory of plates and shells 2nd ed. NewYork: McGraw-Hill;1959.
34. Lin J, Mohamed M, Balint D, Dean TA. The development of continuum damage mechanics-based theories for predicting forming limit diagrams for hot stamping applications. Int J Dam Mech 2014; 23(5): 684-701. doi: 10.1177/1056789513507731
35. Lin J, Liu Y. A set of unified constitutive equations for modelling microstructure evolution in hot deformation. J Mat Process Tech 2003; 143-144: 281-285. doi:10.1016/S0924-0136(03)00472-2

Highlights

- Novel flange wrinkling model for sheet stamping processes with macro-textured tool.
- Hinged boundary condition most accurate tool texture constraint on blank.
- Texture ratio and draw ratio effects are key factors affecting onset of wrinkling.